Nonlinear Modeling of Protein Separation in a Preparative-Scale Dynamic Field Gradient Focusing Instrument

Noah I. Tracy and Cornelius F. Ivory
School of Chemical Engineering and Bioengineering, Washington State University, PO Box 642710, Pullman, WA 99164

DOI 10.1002/aic.11683
Published online November 20, 2008 in Wiley InterScience (www.interscience.wiley.com).

Dynamic field gradient focusing (DFGF) uses an electric field gradient opposed by a counter-flow of buffer to separate milligrams of proteins according to their electrophoretic mobilities. A nonlinear model of protein separation in a preparative-scale DFGF device was developed to aid in refining the instrument's design and finding optimal run conditions prior to performing experiments. The model predicted the focal points of bovine serum albumin (BSA), and bovine hemoglobin (Hb) to within the 95% confidence intervals about the means of the experimental values. The resolution between the proteins in the model was 2.08, which was 3% less than the lower limit of the 95% confidence interval about the experimental value. The model predicted 67% more dispersion than was present in the experimental device, which made the simulated BSA peak 22% wider than the experimentally measured width. © 2008 American Institute of Chemical Engineers *AIChE J,* 55: 63–74, 2009
Keywords: nonlinear modeling, dynamic field gradient focusing, equilibrium-gradient method, preparative electrophoresis, electric field gradient focusing, protein separation

Introduction

Dynamic field gradient focusing (DFGF) simultaneously separates proteins,[1,2,3] or other charged analytes, according to their electrophoretic mobilities and focuses them into discrete bands. The dynamic aspect of DFGF arises from a computer-controlled electric field gradient that can be adjusted as a run progresses, allowing the operator to increase the resolution between two proteins that might not have separated in the original electric field gradient. Separating molecules according to their electrophoretic mobilities could be particularly useful for recombinant, therapeutic proteins, because the various post-translational modifications, e.g., glycosylation and phosphorylation, affect the proteins' biological activities[4,5] and electrophoretic mobilities by altering the proteins' volumes or net charges.

There are two primary reasons why a quantitative, nonlinear model of protein separation in the preparative-scale DFGF instrument was developed. First, it will allow the instrument to be refined further than was possible with the simple linear model originally used to design the device.[6,7] Second, the nonlinear model provides an inexpensive way to quickly test a wide variety of operational settings, and choose optimal conditions prior to physically running a separation in the instrument. Therefore, this article describes a time-dependent, nonlinear model with no fitted parameters that predicts the separation of bovine hemoglobin (Hb), and fluorescein isothiocyanate-labeled bovine serum albumin (FITC-BSA) in the preparative-scale DFGF instrument. The article also compares the nonlinear model's results to those of a linear model and an experimental separation using the same proteins.

Correspondence concerning this article should be addressed to C. Ivory at cfivory@wsu.edu.

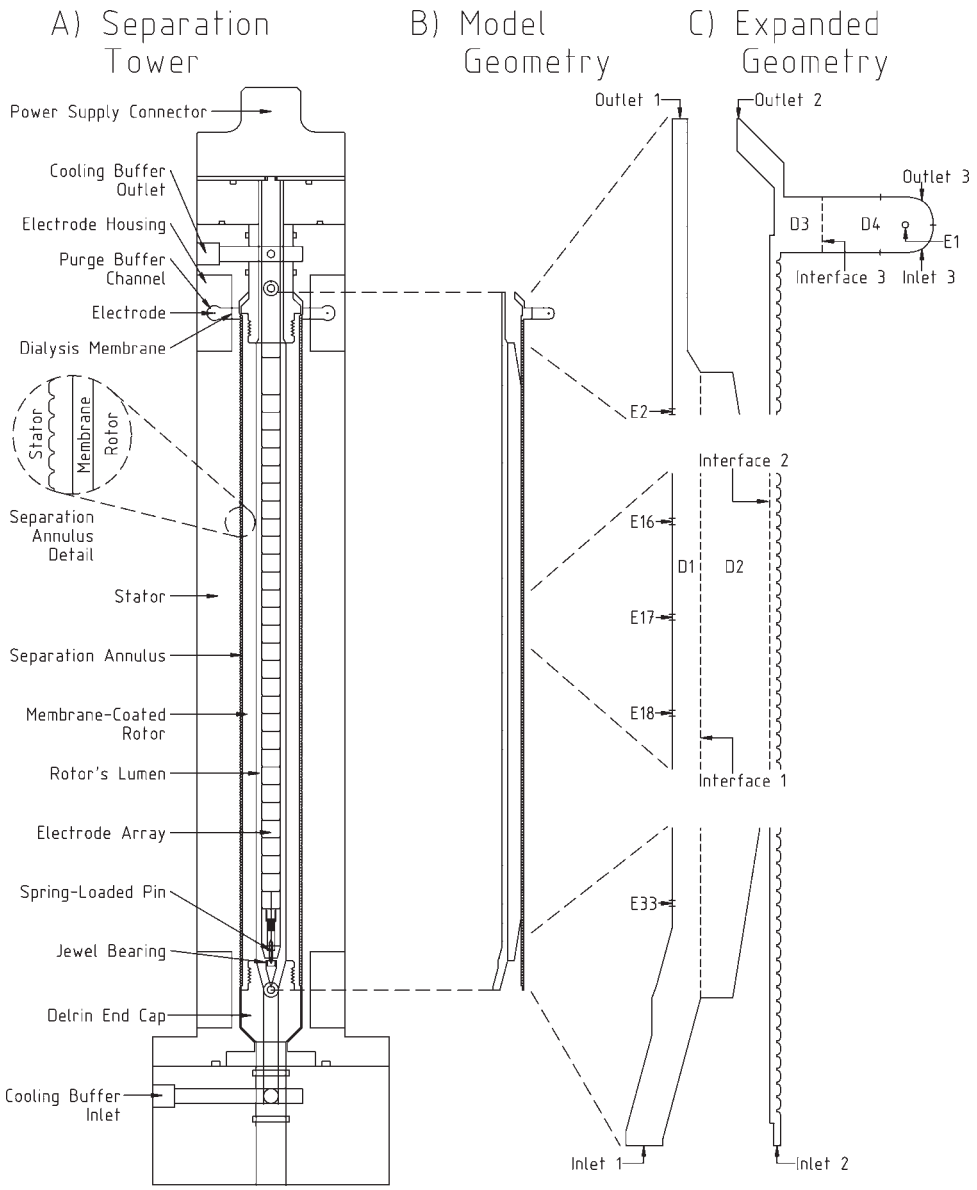

Figure 1. Part A shows a cross-section CAD drawing of the preparative-scale DFGF apparatus' separation tower, and the geometry shown in part B was modeled in axis-symmetric cylindrical coordinates.

Important boundaries are named and shown on the expanded views of the geometry in part C. The 33 electrodes are numbered E1 through E33. The geometry was divided into 4 domains, labeled D1 through D4.

The nonlinear nature of the model presented here arises from the interactions between the electric field gradient and the ions in solution. In linear models, the electric field is unaffected by variations in the conductivity of the solution produced by electromigration, convection, and diffusion. Coupling the ionic concentrations with the electric field allows the model to predict deviations in the electric field gradient that alter the shape and resolution of protein peaks.

In particular, focused protein bands and concentration gradients in the background electrolytes that make up the buffering solution can alter the electric field gradient. Modeling by Humble et al.[8] simultaneously solved for the electric potential and background electrolyte concentrations in a 3-D model of their analytical-scale focusing device; however, the model does not contain any proteins. Their results[8] show that concentration gradients in the buffer electrolytes form within their field gradient focusing device, and that these gradients adversely affect the device's resolving power.

Koegler and Ivory[9] report the effect of focused proteins on the electric field gradient. Regions of decreased conductivity form where the proteins focus and cause the electric field strength to increase within the regions in order to satisfy the conservation of charge. This causes the fronts of the protein peaks to skew forward and the tails to be more diffuse than otherwise expected. The effect of the proteins on the electric field gradient becomes more important as the total amount of protein increases.

Qualitative, transient models of protein focusing in electric field gradients have been published by Koegler and Ivory[9]

and Warnick et al.[10] Warnick and coworkers linearized their model by assuming that the electric field gradient was independent of the ionic concentrations, which let them specify a fixed electric field gradient. Thus, the model only had to solve for the protein's concentration as a function of position and time. Neglecting the effect of ionic concentration on the electric field gradient allowed Warnick et al.[10] develop an approximate, analytical solution to their model. In contrast, the nonlinear model used by Koegler and Ivory[9] allowed for the ionic concentrations to influence the electric field gradient. Koegler and Ivory's model[9] numerically solved for the electric potential and the concentration of a cation, an anion, and two proteins as a function of time and position.

The model presented in this paper followed the nonlinear approach used by Koegler and Ivory[9] and by Humble et al.[8] coupling the ion concentrations and the electric field. The cylindrical, 2-D, axis-symmetric model presented here did not group all ions of like charge together as Koegler and Ivory's model did,[9] nor did it exclude proteins like the model by Humble et al.[8] Instead, the model solved for all species present in the experimental runs, except for hydronium ion, and included equilibrium reactions between buffer species. The hydronium ion was excluded because its was assumed to have little effect on the conductivity of the solution since its concentration was around 100× less than any of the other species at the alkaline pH being modeled. Consequently, pH was calculated by assuming the hydronium ion concentration was equal to the concentration that would be in equilibrium with the hydroxide ion concentration in the model. In addition, the buffer's velocity profile was modeled using a combination of the Navier-Stokes and Brinkman equations[11] in order to account for dispersion in the preparative-scale DFGF instrument. As will be shown, the model quantitatively predicted the focal points of the protein peaks, although the simulated peaks were somewhat wider than the experimental measurements.

Model Development

The preparative-scale DFGF instrument

The prototype preparative-scale DFGF apparatus successfully separated Hb and FITC-BSA.[3] A previous publication describes the many parts of the apparatus: cooling and degassing equipment; a multichannel, computer-controlled power supply; and the DFGF instrument itself, which consists of a base and a separation tower.[7] The following brief description of the construction and operation of the separation tower provides the necessary background for relating the model to the physical device.

The separation tower, shown in part A of Figure 1, contains a hollow, 1.27 cm inner dia., membrane-coated rotor made of a porous, boron nitride ceramic. The membrane on the outer wall of the rotor is approximately 0.25 mm thick, and the membrane-coated rotor has a total outer diameter (OD) of 2.47 cm. The space between the 29.08 cm long ceramic rotor and the 6.35 cm OD transparent acrylic stator forms the separation annulus, which averages 0.762 mm wide. The turning membrane-coated rotor and grooved stator generate counter-rotating vortices that stabilize the axial separation against natural convection at the cost of some radial mixing. Nested within the rotor's lumen is the electrode array, which has 32, 0.25 mm OD platinum wire electrodes that wrap around the 0.762 cm OD body of the electrode array to form rings. The power supply connector attaches the electrode array to an external, computer-controlled, multichannel power supply (Protasis Corporation, Marlborough, MA, USA) which sets the electric field gradient in the separation tower.

A buffer solution fills the rotor's lumen, separation annulus, and the purge buffer channel allowing electrical current to flow radially from the electrode array in the rotor's lumen through the porous rotor, and then vertically up the separation annulus where it then passes through a dialysis membrane, and reaches the two cathodes in the electrode housings at the top of the stator. The polysulfone membrane cast onto the surface of the rotor, and the dialysis membrane that segregates the separation annulus from the purge buffer channel, keep proteins from fleeing the separation annulus and prevent bulk flow between the separation annulus, the cooling buffer, and the purge buffer. Cooling buffer flows up the rotor's lumen and sweeps away electrolysis products formed on the array of platinum electrodes as it cools the separation annulus. The purge buffer that flows over the cathodes removes electrolysis products generated on the cathodes. A small peristaltic pump, not shown in Figure 1, generates the counter-flow that enters the bottom of the separation annulus.

The combination of a counter-flow and an electric field gradient focuses each protein in the separation annulus at the point where the protein's net velocity equals zero, as shown in Figure 2. The counter-flow pushes the Hb and FITC-BSA up the separation annulus with a constant velocity, while the electric field gradient pushes these negatively charged proteins down the separation annulus with electrophoretic velocities that are equal to each protein's electrophoretic mobility multiplied by the electric field strength. The electric field strength is strongest at the top of the chamber and decreases with the height of the separation chamber. Thus, the proteins' net velocity is downwards at the top of the separation annulus, because the electrophoretic velocity exceeds the upwards counter-flow. The net velocity decreases as the proteins move down the separation annulus, and it becomes zero as the proteins reach their focal points where the velocity from the counter flow equals the electrophoretic velocity. Below the focal point the net velocity is upwards because the velocity of the counter-flow exceeds the electrophoretic velocity.

Modeling protein separations in this system required consideration of fluid hydrodynamics in addition to mass conservation of the species in solution. Accordingly, the protein separation model was divided into two parts: a hydrodynamics simulation and a mass-transport simulation. COMSOL Multiphysics v3.3a (COMSOL, Inc., Burlington, MA, USA), a finite-element program for generating meshed geometries and solving partial-differential equations, was used to solve the hydrodynamics and mass-transport simulations in a cylindrical, axi-symmetric, 2-D domain.

Hydrodynamics simulation

The hydrodynamics simulation was solved first and independently of the mass-transport simulation. Doing so neglected any small changes in the fluid properties that might

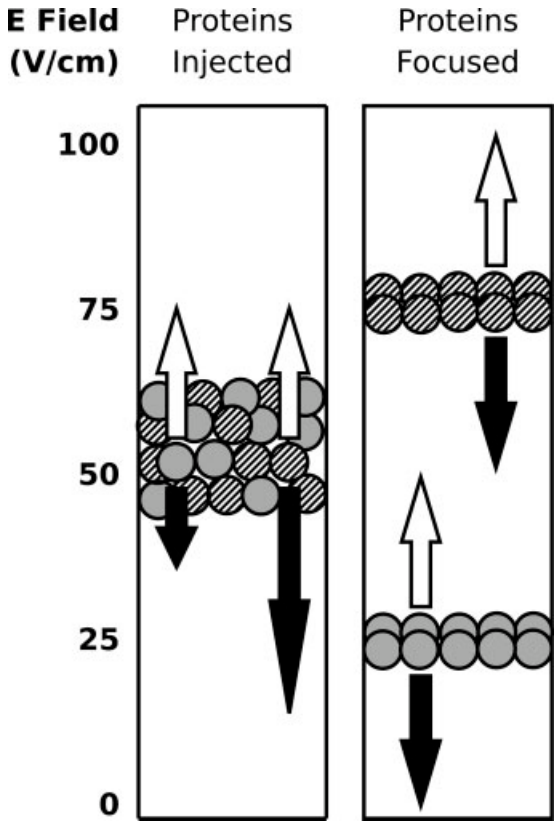

Figure 2. Schematic showing proteins moving from a central injection point to their focal points.

In the left panel, the BSA (gray circles) has a greater mobility than Hb (striped circles), so the electric field imparts a greater downward velocity (black arrows) to the BSA than to the Hb. Both proteins experience a uniform upwards velocity (white arrows) due to the counterflow pumped into the base of the separation chamber. The net velocity on each protein moves it to its focal point, shown in the right panel, where the upward and downward velocities balance each other.

be produced by the focusing ions. Radial electroosmotic flow from Domain 2, the ceramic rotor, into the rotor's lumen, Domain 1, was not included in the hydrodynamics simulation or mass-transport simulation. However, an equivalent radial flow was incorporated by setting the inlet and outlet flows on the separation annulus to match the experimentally measured flow rates of 0.147 mL/min at the inlet, and 0.136 mL/min at the outlet, and allowing the excess buffer to flow through the ceramic and into the rotor's lumen at flow rates determined by the pressure difference between the rotor's lumen and the separation annulus, Domain 3. Specifying the inlet and outlet flow rates for the separation annulus ensured that the net radial flow rate into the rotor during the simulation corresponded to the net radial flow rate of the experiments. There was no way to guarantee that the simulated radial flow rate at any particular height matched the experimental flow rate at that height, because there was no way to measure the radial flow rate at a given height. The velocity profiles from the hydrodynamics simulation were used in solving the mass-transport simulation.

COMSOL Multiphysics allows the user to select various physics, or sets of equations, that describe different physical phenomena, like momentum or mass-transport. The physics specify which governing equations apply to which domains. The Incompressible Navier-Stokes physics was selected to model the flow of the cooling buffer and purge buffers in Domains 1 and 4, which are shown in Figure 1. Choosing the conservative form of the physics forced COMSOL to simultaneously solve a steady-state, velocity form of the Navier-Stokes equation

$$-\nabla \cdot \boldsymbol{\tau} + \rho\, \mathbf{v} \cdot \nabla \mathbf{v} + \nabla p = \rho \mathbf{g} \tag{1}$$

and the continuity equation

$$\nabla \cdot \mathbf{v} = 0, \tag{2}$$

to model the pressure p, along with the r and z components of the velocity vector $\mathbf{v}$. The gravity vector $\mathbf{g}$, contained only a downward z component equal to 9.8 m/s^2. The viscous stress tensor in Eq. 1 is

$$\boldsymbol{\tau} = \eta(\nabla \mathbf{v} + (\nabla \mathbf{v})^T). \tag{3}$$

The density, ρ, and viscosity, η, were held constant at 999.7 kg/m^3 and 1.308×10^{-3} N·s/m^2, respectively. The COMSOL Swirl Flow physics used to model flow in Domain 3, shown in Figure 1, was a variation of the Incompressible Navier-Stokes physics that includes the θ component of flow. The angular component of the flow was required for modeling the vortices that form in the separation annulus. Flow in the porous ceramic rotor, Domain 2 of Figure 1, was modeled using the Brinkman module, which solved the Brinkman equation

$$-\nabla \cdot \boldsymbol{\tau} + \frac{\eta}{\kappa}\mathbf{v} + \nabla p = \rho \mathbf{g} \tag{4}$$

in conjunction with Eq. 2, the continuity equation, to arrive at the r and z velocities within the ceramic. The permeability, κ = 7.35 × 10–17 m^2, was calculated from scaled down experiments (data not shown) measuring radial flow rates at constant pressure drops across short sections of the membrane-coated rotor. It should be noted that Domain 2 includes the polysulfone membrane that coated the ceramic rotor because the measured permeability included any resistance imposed by the membrane.

The boundary conditions for solving equations 1, 2, and 4 were based on the the experimental conditions used to collect the data presented in a previous article.[3] At Inlets 1–3, shown in Figure 1, the velocities are equal to the flow rates entering the boundary divided by the cross sectional area of the inlet. The flow rate at Inlets 1 and 3 was 375 mL/min, while the counter-flow entering Inlet 2 was 0.147 mL/min. Outlet 2 had a fixed flow rate of 0.136 mL/min. Outlets 1 and 3 were given constant pressure boundary conditions. Pressures and velocities in Domains 1–3 were coupled by setting pressures and velocities to be continuous across Interfaces 1 and 2. For example, in the Navier-Stokes module, the pressure at Interface 1 equaled the pressure in the Brinkman module so that the pressure in the simulation was linked between modules. The surfaces labeled Rotor Walls and Interface 2 were also given rotational velocities matching the 60 RPM of the rotor during experiments. Interface 3 represented a dialysis membrane and was considered impermeable to flow because measurements (data not shown) from the

preparative-scale DFGF instrument showed that there was no bulk flow across the membrane. All other surfaces were considered to have no-slip boundary conditions.

In Table 1, which presents the boundary conditions, subscripts r, θ, and z identify the component of a vector. Subscript j denotes the jth species, while subscripts NS, BR, SF and NP stand for the Navier-Stokes, Brinkman, Swirl Flow, and Nernst-Planck physics. In Table 1, bold letters represent vectors, with $\boldsymbol{n}$ being the outward normal vector. The velocities listed in Table 1 have units of m/s.

Mass-transport simulation

The simulation of mass-transport in the preparative-scale DFGF instrument's separation tower was based on assuming species behaved as if they were in an electrically neutral and dilute solution. The former assumption neglected double layer effects that apply within 10–100 angstroms of charged surfaces but do not apply to the bulk solution, while the latter ignored any solute-solute interactions that would have affected the transport of the solutes. As Newman discusses,[12] such assumptions allow models to include the dominant physical processes while avoiding a good deal of complexity. Equilibrium reactions for tris and acetic acid were included in the reaction terms of the mass conservation equations to properly predict the conductivity of the solution. The pH dependence of the proteins' net charges was not included at this time due to lack of computing power. Each charge state would have added another unknown to solve for and the current model already used all 4 GB of RAM on our quad-core Dell 390 work station (Dell Computers, Austin, Texas, USA). Including more of the proteins' charge states, at the cost of some of the current carrying species, would have altered the simulated system to the extent that it would be unlikely to accurately model the experimental system.

The simulation included all the ions used in the experiment: tris base in neutral (Tris) and ionized ($Tris^+$) forms, undissociated (Ac) and dissociated (Ac^-) acetic acid, ionized cetyltrimethylammonium (CTA^+) bromide (Br^-) and sodium (Na^+) dodecylsulfate (DS^-), hydroxide (OH^-), Hb (Hb), and FITC- BSA (BSA). The tris and acetate provided buffering at pH 8.8, while the surfactants maintained a positive surface charge on the porous rotor so that electro osmotic flow would be directed into the rotor's lumen. Following Humble et al.[8] the hydronium ion was left out of the model because at pH 8.8, the pH of the experiment that was modeled, the concentration of hydronium ion was two-orders of magnitude less than any other ion; so it contributed little, if at all, to the conductivity of the buffer. Including the proteins in the mass transport simulation, and limiting them to Domain 3, the separation annulus, required that the simulation use two separate Nernst-Planck physics because COMSOL requires that species within a physics be present in all domains that the physics applies to. Therefore, Nernst-Planck physics 1 contained all species except the proteins and applied to Domains 1,2, and 4. Nernst-Planck physics 2 included all species and applied to Domain 3. The physics were coupled by setting the concentrations and fluxes of each species in Nernst-Planck physics 1 equal to the corresponding species in Nernst-Planck physics 2 at Interfaces 2 and 3.

Table 1. Boundary Conditions for Fluid Mechanics and Mass-Transport Simulations

	Hydrodynamics Simulation			Mass-Transport Simulation	
Surface	Navier-Stokes Physics (Domains 1, 4)	Brinkman Physics (Domain 2)	Swirl Flow Physics (Domain 3)	Nernst-Planck Physics 1 (Domains 1, 2, 4)	Nernst-Plank Physics 2 (Domain 3)
Inlet 1	$\mathbf{v}_r = 0, \mathbf{v}_z = 0.1973$	–	–	c_j = initial value, $\mathbf{n} \cdot \mathbf{i} = 0$	–
Inlet 2	–	–	$\mathbf{v}_r = 0, \mathbf{v}_\theta = 0, \mathbf{v}_z = 5.311\text{E}-5$	–	c_j = initial value, $\mathbf{n} \cdot \mathbf{i} = 0$
Inlet 3	$\mathbf{v}_r = 0, \mathbf{v}_z = 0.1973$	–	–	c_j = initial value, $\mathbf{n} \cdot \mathbf{i} = 0$	–
Outlet 1	$p = 0, \tau \cdot \mathbf{n} = 0$	–	–	$\mathbf{n} \cdot (\mathbf{N}_j - c_j \mathbf{v}) = 0, \mathbf{n} \cdot \mathbf{i} = 0$	–
Outlet 2	–	–	$\mathbf{v}_r = 0, \mathbf{v}_\theta = 0, \mathbf{v}_z = 1.467\text{E}-4$	–	$\mathbf{n} \cdot (\mathbf{N}_j - c_j \mathbf{v}) = 0, \mathbf{n} \cdot \mathbf{i} = 0$
Outlet 3	$p = 0, \tau \cdot \mathbf{n} = 0$	–	–	$\mathbf{n} \cdot (\mathbf{N}_j - c_j \mathbf{v}) = 0, \mathbf{n} \cdot \mathbf{i} = 0$	–
Interface 1	$p = p_{BR}, \tau \cdot \mathbf{n} = 0$	$\mathbf{v}_r = \mathbf{v}_{r,NS}, \mathbf{v}_z = \mathbf{v}_{z,NS}$	–	–	–
Interface 2	–	$p = p_{SF}, \tau \cdot \mathbf{n} = 0$	$\mathbf{v}_r = \mathbf{v}_{r,BR}, \mathbf{v}_\theta = 2\pi r, \mathbf{v}_z = \mathbf{v}_{z,BR}$	$-\mathbf{n} \cdot \mathbf{N}_j = \mathbf{n} \cdot \mathbf{N}_{j,NP2}, -\mathbf{n} \cdot \mathbf{i} = \mathbf{n} \cdot \mathbf{i}_{NP2}$	$c_j = c_{j,NP1}, \Phi = \Phi_{NPI}$
Interface 3	$\mathbf{v}_r = 0, \mathbf{v}_z = 0$	–	$\mathbf{v}_r = 0, \mathbf{v}_\theta = 0, \mathbf{v}_z = 0$	$-\mathbf{n} \cdot \mathbf{N}_j = \mathbf{n} \cdot \mathbf{N}_{j,NP2}, -\mathbf{n} \cdot \mathbf{i} = \mathbf{n} \cdot \mathbf{i}_{NP2}$	$c_j = c_{j,NPI}, \Phi = \Phi_{NPI}$
Electrode 1	$\mathbf{v}_r = 0, \mathbf{v}_z = 0$	–	–	c_j = initial value, $\Phi = -200V$	–
Electrode 2	$\mathbf{v}_r = 0, \mathbf{v}_z = 0$	–	–	c_j = initial value, $\Phi = 0V$	–
Electrode 3–33	$\mathbf{v}_r = 0, \mathbf{v}_z = 0$	–	–	c_j = initial value, $\Phi = \Phi_{set}$	–
Rotor Walls	–	–	$\mathbf{v}_r = 0, \mathbf{v}_\theta = 2\pi r, \mathbf{v}_z = 0$	–	$\mathbf{n} \cdot \mathbf{N}_j = 0, \mathbf{n} \cdot \mathbf{i} = 0$
All Others	$\mathbf{v}_r = 0, \mathbf{v}_z = 0$	$\mathbf{v}_r = 0, \mathbf{v}_z = 0$	$\mathbf{v}_r = 0, \mathbf{v}_\theta = 0, \mathbf{v}_z = 0$	$\mathbf{n} \cdot \mathbf{N}_j = 0, \mathbf{n} \cdot \mathbf{i} = 0$	$\mathbf{n} \cdot \mathbf{N}_j = 0, \mathbf{n} \cdot \mathbf{i} = 0$

Table 2. Physical Constants for Mass-Transport Simulation

Species	Limiting Conductivity ($\times 10^{-8}$ cm^2·s/mol)	Diffusion Coefficient ($\times 10^{-10}$ m^2/s)	Absolute Mobility[a] ($\times 10^{-13}$ mol·s/kg)	Charge	Initial Value (mM)
Neutral Tris (Tris)	29.2[15]	7.64	3.14	0	8.34
Ionized Tris ($Tris^+$)	29.2[15]	7.64	3.14	1	1.66
Neutral Acetic acid (Ac)	40.9[16]	10.7	4.39	0	1.51×10^{-4}
Ionized Acetic Acid (Ac^-)	40.9[16]	10.7	4.39	−1	1.66
Cetyltrimethylammonium (CTA^+)	20.9[16]	5.47	2.25	1	0.105
Bromide (Br^-)	78.1[16]	20.4	8.39	−1	0.105
Sodium (Na^+)	50.08[16]	13.1	5.38	1	Calculated by COMSOL
Dodecylsulfate (DS^-)	24.0[16]	6.28	2.59	−1	0.035
Hydroxide (OH^-)	198[16]	51.8	21.3	−1	6.331×10^{-3}
Hemoglobin (Hb)	–	0.658[14]	0.09	−7.72[17]	$0.0944e^{-1000\left(\frac{z-0.145}{0.29083}\right)^2}$
FITC-BSA (BSA)	–	0.594[13]	0.09	−(21.36[13] + 1[3])	$0.0965e^{-1000\left(\frac{z-0.145}{0.29083}\right)^2}$

[a]COMSOL uses absolute mobility [mol s/kg], rather the more familiar electrophoretic mobility [m^2/V s]. Equation 11 gives the relationship between the two mobilities.

The conservative mode of the Nernst-Planck module uses a transient (t = time) conservation equation

$$\frac{\partial c_j}{\partial t} + \nabla \cdot \mathbf{N_j} = R_j \tag{5}$$

for the species concentrations c_j, based on the flux $\mathbf{N_j}$, and a homogeneous reaction term R_j. The flux for each species was defined as

$$\mathbf{N_j} = -D_j \nabla c_j - z_j u_j F c_j \nabla \Phi + c_j \mathbf{v} \tag{6}$$

where D_j is the diffusivity; Z_j is the charge on each species; u_j is the absolute mobility; $\boldsymbol{F}$ is the Faraday constant; $\boldsymbol{\Phi}$ is the electric potential; and $\mathbf{v}$ is the velocity, which was previously determined by the hydrodynamics simulation. However, one of n total species is solved for by means of electroneutrality

$$\sum_{j=1}^{n} \left(z_j c_j\right) = 0 \tag{7}$$

rather than by its conservation equation because only the concentrations of $n - 1$ species are independent. An equation for the conservation of charge using the current density $\boldsymbol{i}$

$$\nabla \cdot \mathbf{i} = F \sum_{j=1}^{n} z_j \boldsymbol{R_j} \tag{8}$$

accounts for the electric potential Φ. The current density in Eq. 8 is defined by

$$\mathbf{i} = \boldsymbol{F} \sum_{\boldsymbol{j=I}}^{\boldsymbol{n}} \boldsymbol{z_j} \mathbf{N_j} \tag{9}$$

The conservation equation, Eq. 5, for $n - 1$ species are solved simultaneously with the current conservation equation, Eq. 8, to determine the concentrations of all the ions and the electric potential throughout the domains. Na^+ was chosen as the species calculated by the electroneutrality equation, because it had a positive charge and was not involved in equilibrium reactions.

The diffusion coefficients were found in the literature,[13,14] or calculated from limiting conductivities. All diffusion coefficients were multiplied by the porosity of the rotor, which is 14% in Domain 2, to account for the resistance to diffusion caused by the ceramic rotor. Diffusion coefficients for the proteins, shown in Table 2, were also found in the literature.[13,14] The diffusion coefficients for the other species are shown in Table 2 and were calculated from limiting conductivities,[15,16] λ_j, using

$$D_j = \frac{R_g T}{F^2} \frac{\lambda_j}{|z_j|} \tag{10}$$

where R_g is the gas constant; T is the absolute temperature; and F is Faraday's constant. Diffusion coefficients were calculated at 20 C, because the protein data was at 20 C.

Electrophoretic mobility and limiting conductivity data were used to calculate the absolute mobilities u_j, at 20 C for the species shown in Table 2. In the case of the proteins, absolute mobilities were calculated using the equation

$$u_j = \frac{\mu_j}{z_j F} \tag{11}$$

with titration data[13,17] and experimental values[18] of electrophoretic mobilities μ_j. As stated earlier, charge variation with pH could not be included in the model due to limited RAM available on the workstation solving the model. Therefore, protein charges were calculated at pH 8.3, because that was the pH of the protein-laden fractions collected during prior experimental work.[3] Also, the charge of the BSA was adjusted by −1 to account for the one negatively charged FITC molecule attached[3] to each BSA molecule. Absolute mobilities of the other ions were calculated from limiting conductivity data by the equation

$$u_j = \frac{\lambda_j}{F^2 |z_j|} \tag{12}$$

The reaction terms were set to zero for the surfactants and the proteins. For the buffering species, the reaction terms were derived from the equilibrium relations between species. The equilibrium equation for acetic acid was

$$K_{b,Ac} = \frac{c_{Ac} c_{OH^-}}{c_{Ac^-}} = \frac{k_{f,Ac}}{k_{r,Ac}} \tag{13}$$

where K_b is the base equilibrium constant and k_f and k_r were the forward and reverse rate constants. A similar equilibrium relationship applied to the tris

$$K_{b,Tris} = \frac{c_{Tris} - c_{OH^-}}{c_{Tris}} = \frac{k_{f,Tris}}{k_{r,Tris}} \tag{14}$$

The base equilibrium constants for acetic acid and tris were calculated from tabulated[16] pKa values. Equations 12 and 13 were used to write the following homogeneous reaction terms R_j, for the ions involved in buffering reactions

$$R_{Ac} = -R_{Ac^-} = k_{r,Ac}\left(K_{b,Ac}c_{Ac^-} - c_{Ac}c_{OH^-}\right) \tag{15}$$

$$R_{Tris^+} = -R_{Tris} = k_{r,Tris}\left(K_{b,Tris}c_{Tris} - c_{Tris^+}c_{OH^-}\right) \tag{16}$$

and

$$R_{OH^-} = R_{Ac} + R_{Tris^+} \tag{17}$$

The reverse rate constants, k_r, defined for tris and acetic acid were incrementally raised during preliminary simulations until they were set to 1,000. At those values, the reaction rates were fast enough so that concentrations deviated from equilibrium by less than 1%. Unlike Humble et al.[8] we did not notice any numerical instability while increasing the reaction rate.

The boundary conditions for the mass-transport simulation, Eqs. 5–7, are listed in Table 1 and correspond to the conditions of the experimental protein separations.[3] The species concentrations were set to constant values at Inlets 1–3 to mimic the constant flow of buffer into the apparatus. Outlets 1–3 used convective flux boundary conditions for the species, assuming that hydrodynamic flow was chiefly responsible for carrying the species out of the experimental apparatus. Electrode reactions were neglected on the assumption that the fast buffering reactions and flow rate would remove any buildup of ions near the electrodes. Therefore, the concentrations at the electrode surfaces were set to the inlet concentrations.

Boundary conditions for the electrical potential also matched the experimental conditions.[3] The voltage setting on the electrodes, E3–E33, in the model was calculated using the formula

$$\Phi_{set} = -12038\mathrm{z}^2 + 482.25\mathrm{z} + 785.68\mathrm{V} \tag{18}$$

which was equivalent to the electrode settings used during the separation experiments. The cathode, E1, was set to -200 V and E2 was set to 0 V, as was done in the experiments. All other boundaries in the simulation were electrically insulated because electrical current only entered or left the experiment via the electrodes.

The mass-transport simulation also required the use of isotropic artificial diffusion for all species in Domains 1, 3, and 4. Using artificial diffusion dampened oscillations in the solution, particularly at boundaries and the interfaces between physics where the gradient of the solution was steep. The oscillations, which had prevented the solver from converging, occurred because the finite element mesh could not be infinitely refined near the borders and interfaces due to the limited amount of RAM in the workstation running COMSOL. A complete description of how COMSOL applies artificial diffusion can be found in the COMSOL Multiphysics User's Guide that comes with the software. The following brief explanation should convey the general concept. The amount of artificial diffusion varies locally on the mesh with the element size and the convective velocity. Hence, artificial diffusion is only added where the mesh elements are large, or the convective velocity is fast. For example, the area-averaged artificial diffusion added to Am^- with the artificial diffusion tuning parameter set to 0.5 was approximately 1.1E-10 m^2/s in Domain 3 where the flow rates were small and the mesh tightest. In Domain 1, where the velocity was greatest and the mesh elements the largest, an average of 7.5E-7 m^2/s was added to the diffusion coefficient of Am^-. The large addition to the Am^- diffusion coefficient in Domain 1 still left the diffusive contribution to the flux of Am^- about eight-orders of magnitude less than the convective contribution. Thus, the artificial diffusion smoothed out the oscillation in the solution while still leaving the flux of Am^- in Domain 1 dominated by convection.

Solution procedure

After setting up the governing equations and boundary conditions in COMSOL Multiphysics, as described in the previous two sections, finite element meshes were generated and the simulations performed. The mesh for the hydrodynamics simulation was created using the Normal setting, and by making the minimum element size equal to 1.5E-4 on Interface 1 and 2. The resulting mesh had 106592 elements and 3044752 degrees of freedom. The steady-state solution for the hydrodynamics simulation was found using the parametric UMFPACK solver and ramping the density of the buffer from 0 to 999.7 kg/m^3. Starting the simulation with the density equal to zero provided a linear system which was easily solved and used as the trial solution for a slightly nonlinear system with density equal to 10 kg/m^3. Then, the slightly nonlinear solution served as the guess for a more nonlinear system, and so on, until the simulation was performed with the density set to 999.7 kg/m^3. The velocity profiles from the hydrodynamics simulation were saved for use in the mass-transport simulation. Attempting to solve the mass-transfer simulation using the mesh developed for the hydrodynamics simulation consumed more memory than was available on the workstation and crashed the program. Therefore, a less dense mesh was generated for the mass-transport model by choosing the Coarser mesh setting, and limiting the maximum element size to 1E-3. The new settings produced a mesh with 19960 elements and 547465 degrees of freedom. The transient mass-transport simulation was solved from 0–7,200s using the PARDISO solver with the Nested Dissection preordering algorithm.

Results and Discussion

The goal of simulating fluid flow and mass-transport in the preparative-scale DFGF instrument was to arrive at a quantitative model of protein separation in the device. The velocity profiles throughout the separation tower were specified by the solution to the hydrodynamics model. The mass-transport simulation built on the results of the hydrodynamics simula-

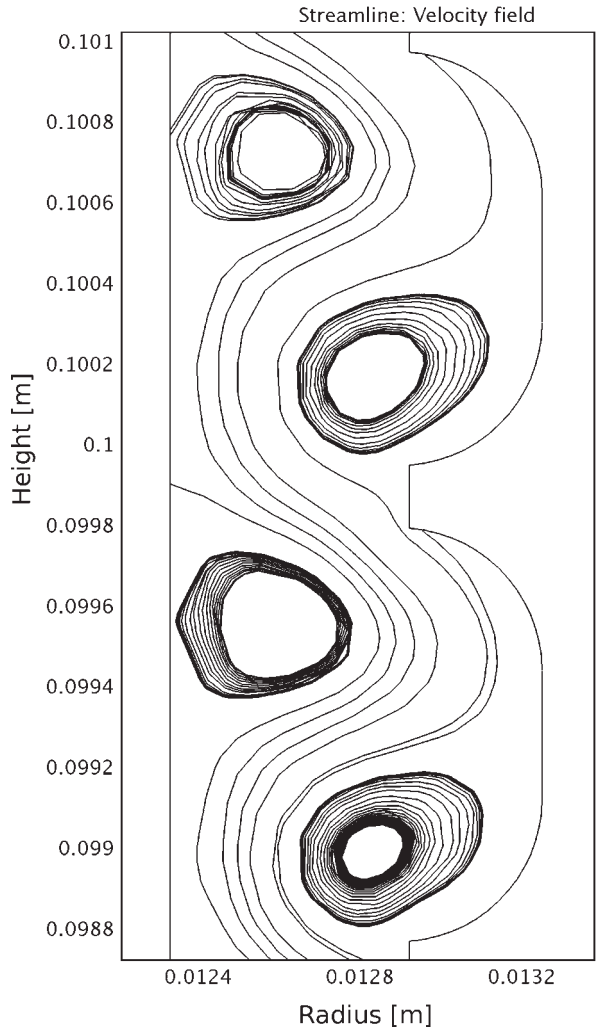

Figure 3. The streamlines show the velocity field in the separation annulus.

The vortices near the ceramic rotor's outer wall, on the left, rotate counter-clockwise while those on the right, near the shaped stator wall, turn clockwise. The axial flow winds its way up the middle of the separation annulus between the vortices.

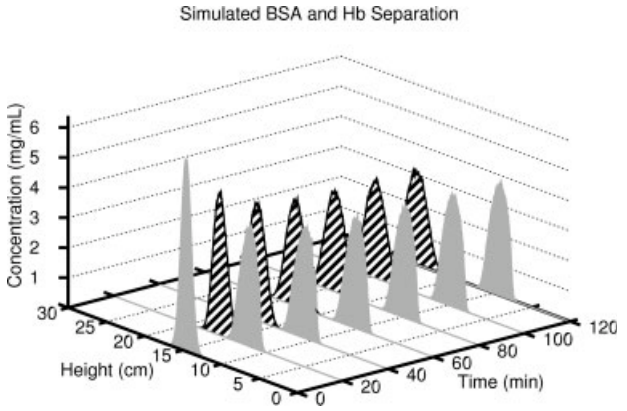

Figure 4. Seven milligrams each of FITC-BSA (gray peak) and Hb (striped peak) are centered near 15 cm when the simulation starts.

By 40 min, the proteins are base-line resolved, and the resolution increases to 2 by the end of the simulation.

Simulating mass transfer in the preparative-scale DFGF instrument under conditions analogous to experimental conditions[3] took about 1.5 hours and yielded the separation shown in Figure 4. The conductivity and pH profiles in the separation annulus are shown in Figure 5. Both the simulation and the experiment started with 7 mg each of BSA and Hb injected into the center of the separation annulus. Hemoglobin and BSA were base-line resolved in about 40 simulated minutes. The simulation ended after two hours, the point at which the experimental runs ended. The model was also tested with proteins having smaller charge differences than the difference between Hb and FITC-BSA, while leaving all the other simulation conditions the same. There was no separation of the two proteins in the simulation after two hours when they had a single charge difference, i.e., −7.72 and −8.72. Increasing the charge on the second charge to −12.72 produced baseline resolution of the proteins by the end of the 2 h simulation, rather than within 40 min as seen with Hb and FITC-BSA in Figure 4.

tion and showed where the proteins focused in the preparative-scale DFGF instrument. The results of the mass-ransport model were compared to experimental results[3] to judge the model's accuracy.

The result of the hydrodynamics simulation was vital to the protein separation model because the convective flow of the buffer in the separation annulus opposed the electrophoretic motion of the proteins so that they would focus. The simulated flow of cooling buffer in the rotor's lumen had a Reynold's Number of 200, as calculated according to Bird and Meter,[19] which suggested that the flow within the rotor's lumen was laminar. The more important result, however, was in the separation annulus. Figure 3 shows that vortices formed in the separation annulus, even with the counter-flow present. The vortices were somewhat distorted by the axial counter-flow, compared to those[20] in the absence of an axial flow.

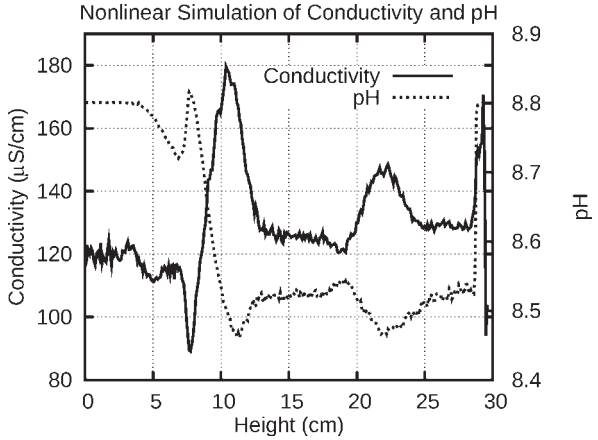

Figure 5. The conductivity and pH in the separation annulus at the end of the simulation.

Table 3. Protein Peak Properties

	Linear Simulation	Nonlinear Simulation	Experiment, Mean of 3 Runs	95% CI about Experimental Mean
BSA Focal Point [cm]	9.75	9.30	10.1	±1.34
Hb Focal Point [cm]	16.0	20.1	19.2	±2.10
BSA Peak Width [cm]	3.00	4.92	4.03	±0.402
Hb Peak Width [cm]	1.73	5.51	2.87	±0.898
Resolution	2.45	2.08	2.64	±0.503

The resolution Rs, between the two proteins is the distance between the protein peak centers, ΔZ, divided by the average of the peak's widths,[21] and is calculated using

$$Rs = \frac{\Delta Z}{4\sigma_{Avg}}, \tag{19}$$

where σ_{Avg} is the average standard deviation in width of the two peaks. Table 3 lists the focal point and peak width of the two proteins at the end of the run, in addition to the resolution between them. These values were calculated based on the width of the peaks at half height, just as the experimental values were calculated,[3] in order to maintain comparability between the simulated and experimental separation.

The focal points and peak widths were determined by assuming the peaks were Gaussian. Thus, the standard deviation in width for each peak related to the peak width at half-height W_h, for each peak by the formula[22]

$$w_h = 2\sigma\sqrt{2\ln 2} = 2.355\sigma \tag{20}$$

The half height for each peak was the difference between the maximum peak height and the baseline.[22] Next, the average standard deviation in Eq. 19 was

$$\sigma_{Avg} = \frac{\sigma_{BSA} + \sigma_{Hb}}{2} \tag{21}$$

where the subscripts indicate which protein the standard deviation belongs to. Peak centers were taken to be at the point that divided W_h in two. The confidence intervals about the experimental means were based on a Student t distribution with n − 1 = 2 degrees of freedom.

Next, the results of the nonlinear mass-transport simulation were compared to the experimental protein separation, and a linear mass-transport simulation where the electric field was uncoupled from the influence of the ionic concentration profiles. The linear model was equivalent to the nonlinear model in all other respects. Figure 6 plots the simulated protein concentrations after 2 h compared to the average concentration profile of three experimental separations performed previously.[3] The experimental curves were produced by measuring pixel intensity along the center of the rotor in digital photographs taken at the end of each run.[3] The large degree of overlap between the protein peaks of the experiment and nonlinear simulation in Figure 6 suggests that the nonlinear model reasonably predicted the proteins' focal points. The linear model only accurately predicted the focal point of the FITC-BSA peak and, as seen in Figure 6, clearly failed to generate realistic peak widths for either protein. The Hb peak in the nonlinear simulation appeared nearly twice as wide as the corresponding experimental peaks, although it was close to the average. The width of the BSA peak in the nonlinear simulation appeared much closer to the width of the experimental BSA peaks. Table 3 compares the focal points and widths of the simulated peaks to the experimental values.

The linear model only predicted the focal point of the FITC-BSA peak to within the uncertainty in the experimental data. The widths of the peaks in the linear simulation were well outside the 95% confidence interval of the mean experimental peak width. Coincidentally, the linear model predicted the resolution between the proteins to within the confidence interval about the mean experimental resolution. This occurred because the linear model predicted such narrow peaks.

The focal points of the peaks in the nonlinear simulation were within the 95% confidence intervals about the the means of the experimental focal points, confirming that the nonlinear model predicted where the proteins should focus in the separation annulus. The nonlinear model did not, however, predict the widths of the protein peaks with the same degree of accuracy. The width of the simulated BSA peak was 22% larger than the mean of the experimental width, and 10% larger than the maximum value allowed by the 95% confidence interval. In the case of Hb, the simulation predicted a band that was 92% too wide, compared to the experimental measurements. The large widths caused the simulated resolution, 2.08, to fall just outside the lower limit, 2.14, of the confidence interval around the mean experimental resolution.

Initially, the use of artificial diffusion in the simulation was thought to cause the BSA peak's slightly larger predicted width. Using artificial diffusion added about 5E-11 m^2/s to BSA's diffusion coefficient in the region where BSA focused, which is substantial compared to BSA's diffusion coefficient of 6.58E-11 m^2/s. The model would not solve without the use of artificial diffusion, nor would it solve with smaller values than those used, so it was difficult to evaluate the extent that artificial diffusion was affecting the peak width.

An alternative approach was to use the information from the simulation to calculate a peak width without the contribution of artificial dispersion. To do this, the BSA peak was considered Gaussian, with variance, σ^2, given by[9]

$$\sigma^2 = \frac{D_{tot,BSA}}{|z_{BSA}u_{BSA}F\nabla\Phi|} \tag{22}$$

where $D_{tot,BSA}$ represents the sum of the BSA's diffusion coefficient, the artificial diffusion $D_{art,BSA}$, and the axial dispersion $D_{disp,BSA}$, generated by the mixing action of the stabilizing vortices. The slope of the simulated electric field gradient on either side of the BSA peak, 23908 V/m, was used with the variance from the simulation and other known

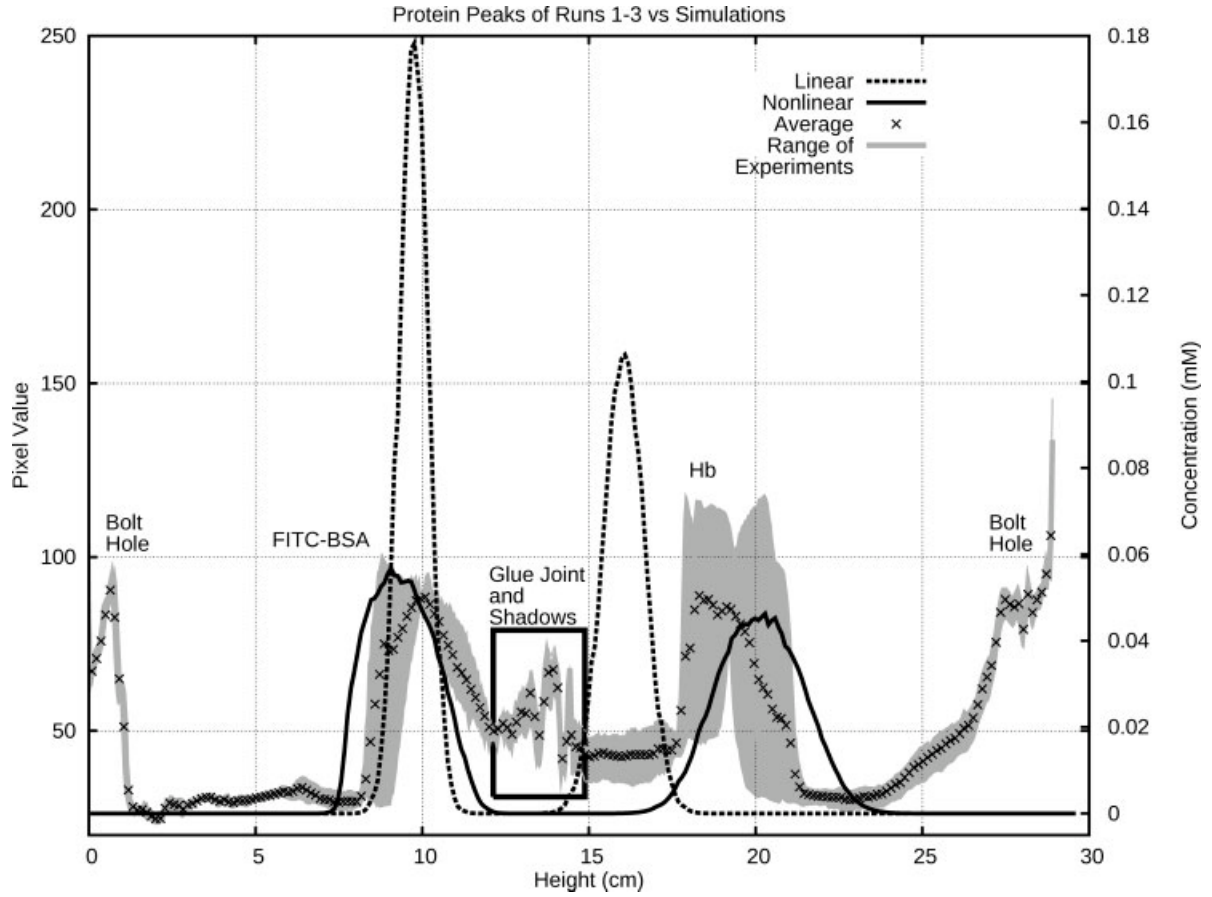

Figure 6. After 2 h of experimental and simulated time, the focal points of the simulated peaks from the linear model (dashed line) are far narrower than the average of the experimental values (X's).

The gray shaded region shows the range of the experimentally measured concentration profiles. In contrast to the linear model, the widths of the peaks from the nonlinear simulation (solid line) more closely resemble the experimental average. The nonlinear simulation also more accurately predicts the experimental focal points of the proteins than does the linear model. The experimental runs were performed on different days with 7 mg each of Hb and FITC-BSA. Bolt holes, a glue joint, and some shadows that extended through the transparent stator caused unusually dark spots in the photographs taken at the end of the experiments. These dark spots showed up as the other labeled peaks. The right axis is for the simulations.

values to calculate a value of 7E-8 m^2/s for $D_{disp,BSA}$. Recalculating BSA's peak width without including the contribution of artificial diffusion decreased the peak width by only 1%. This suggested that the artificial diffusion was not responsible for the discrepancy in peak width between the simulation and the experiments.

As a check, the axial dispersion in the experimental measurements was estimated, as done previously, using the variance from the experimental BSA peak, the slope of the simulated electric field gradient, and without artificial diffusion. The value of axial dispersion in the experiment was 4.7E-8 m^2/s. Thus, the difference between the experimental and simulated BSA peak widths was due to the hydrodynamics simulation predicting more convective mixing than existed in the actual device.

The width of the simulated Hb peak also differed from the experimentally measured width. However, the extra dispersion introduced by the model did not completely explain the discrepancy. The 22% increase in peak width due to the artificial diffusion only accounted for 24% of the difference between the simulated and experimental Hb peak width. Another possible cause for the exceptionally wide peak was the lack of charge dependence on pH in the model. However, the fixed charges assigned to the proteins were based on the pH of protein-laden fractions recovered at the end of experimental runs. Therefore, the absence of charge dependence on pH in the model shouldn't have affected the proteins' focal points or peak widths in this simulation.

As discussed in a prior article[3] the experimental Hb peak width was much narrower than expected because an ion-depleted region of low-conductivity formed at the top of the separation annulus. The size of the region grew from the top of the chamber downward during the run as ions migrated from the top of the separation annulus into the purge channel faster than they were replenished by ions entering the separation annulus in the counterflow buffer or migrating through the rotor from the cooling buffer. The decreased conductivity caused an increase in the local electric field strength, making the field gradient steeper where the Hb focused so that the Hb peak was narrower than the BSA peak.

Other workers[8] in the field have suggested that the formation of ion-depleted regions requires an imbalance of ion

transport into, and along, the axis of the separation chamber. Therefore, we modified the model presented here to include unbalanced transport through the positively charged ceramic rotor by retarding the passage of cations and enhancing the flow of anions. Preliminary results from our modified model showed the formation of an ion-depleted region at the top of the separation annulus (results not shown). Unfortunately, the modified version of the model that included unbalanced transport through the rotor was unsuitable for publication at this time. The modeling workstation does not have enough memory to solve the modified model with finer meshes, and, thus, verify the convergence of the solution. Even so, the results of the nonlinear model presented here, taken together with those of Humble et al.[8] suggest that accounting for the electrostatic effects on ion transport through the ceramic rotor in the preparative-scale DFGF instrument will improve the quantitative model of DFGF.

Concluding Remarks

The simulation of hydrodynamics and mass-transport in the preparative-scale DFGF instrument was intended to quantitatively model protein focusing in the device. A quantitative model of the instrument allows the design to be further refined and optimal experimental running conditions to be found more quickly. The nonlinear simulations of hydrodynamics and mass-transport employed no fitted parameters and correctly predicted the focal points of FITC-BSA at 9.30 cm and Hb at 20.1 cm. The focal points were within the 95% confidence intervals about the means of the experimental focal points. The calculated resolution of 2.08 between the BSA and Hb peaks was within 3% of the lower limit of the 95% confidence interval about the mean of the experimental resolution.

The simulations did not correctly predict the widths of the protein peaks, which pushed the resolution outside the experimental confidence interval, despite the accuracy of the focal points. The hydrodynamics model predicted 67% more dispersion in the separation annulus than was present in the actual experiments, which made the simulated BSA peak wider than the experimental one. The extra dispersion adversely affected the simulated width of the Hb peak, but the real problem was the formation of an ion-depleted region during the experiments which increased the slope of the electric field gradient near the Hb peak, and made the peak particularly narrow in comparison with the simulated peak width.

The modified nonlinear model mentioned in the results section includes unequal transport through the preparative-scale DFGF instrument's rotor. However, the cause of the difference in axial dispersion between the simulation and the experiment needs to be found and removed. These improvements will be particularly important for parametrically testing design changes intended to increase the resolving power of the instrument. Usefully implementing the improved model will require a workstation with more memory; 8 GB might be sufficient, but 16 GB may be necessary to implement the tighter meshes required to verify that the solution is converging.

Presently, the rotor limits the performance of the preparative-scale DFGF instrument, as shown by the combination of results from the modified model mentioned in this paper, the model of Humble et al.[8] and the prior experimental work.[3] The rotor should be redesigned to minimize ion-selective transport through the rotor, which will then reduce the formation of the ion-depleted region. One possible design might consist of a dialysis membrane attached to a plastic support, provided a way can be found to seal the membrane to the plastic support while preventing the membrane from expanding, or bulging, when the cooling buffer flows through the rotor's lumen.

The nonlinear model of preparative-scale DFGF and the other field gradient focusing models cited in the introduction illustrate how the development of more powerful mathematical software and ever-increasing computer power are narrowing the gap between simulated results and experimental ones. For example, the earlier model by Koegler and Ivory[9] produced qualitatively correct results in a relatively simple 1D geometry, whereas the nearly quantitative model described here had a complex 2-D geometry. The modeling and computing power available to current researchers allows for much better agreement between models and experiments so that Humble et al.[8] and Burke and Ivory[23] could use nonlinear models to design defects out of their focusing devices. Likewise, the model developed in this article will be used to test design changes in the preparative-scale DFGF prior to physically implementing them.

Improving the rotor design with the help of the nonlinear model should enhance the resolving power of the preparative-scale DFGF instrument. Currently, it can separate proteins that have at least a charge difference of 5, according to the model presented here (simulations not shown). However, the more refined vortex-stabilized electrophoresis chamber[20] operating in IEF mode separates proteins that differ by only 1 charge.[24] We expect that the preparative-scale DFGF instrument will eventually achieve separations similar to the preparative IEF results in the vortex-stabilized electrophoresis chamber, but with real-time control of the resolution and fewer solubility problems.

Acknowledgments

We thank the Washington State University National Institutes of Health Protein Biotechnology Training Program (grant T32GM08336), the National Science Foundation (grant BES 9970972), and Berlex Laboratories (now a subsidiary of Bayer HealthCare Pharmaceuticals) for funding.

Literature Cited

1. Huang Z, Ivory CF. Digitally controlled electrophoretic focusing. *Anal Chem*. 1999;71:1628–1632.
2. Myers P, Bartle KD. Towards a miniaturised system for dynamic field gradient focused separation of proteins. *J Chromatogr A*. 2004;1044:253–258.
3. Tracy NI, Ivory CF. Protein separation using preparative-scale dynamic field gradient focusing. *Electrophoresis*. 2008;29:2820–2827.
4. Gerngross TU. Advances in the production of human therapeutic proteins in yeasts and filamentous fungi. *Nat Biotechnol*. 2004;22:1409–1414.
5. Voet D, Voet JG. *Biochemistry*. 2nd ed. New York: John Wiley & Sons; 1995.
6. Tracy NI, Ivory CF. Assessing the scalability of dynamic field gradient focusing using linear modeling. *J Sep Sci*. 2007;31:341–352.

7. Tracy NI, Huang Z, Ivory CF. Design and construction of a preparative-scale dynamic field gradient focusing apparatus. *Biotechnol Prog*. 2008;24:444–451.
8. Humble PH, Harb JN, Tolley HD, Woolley AT, Farnsworth PB, Lee ML. Influence of transport properties in electric field gradient focusing. *J Chromatogr A*. 2007;1160:311–319.
9. Koegler WS, Ivory CF. Field gradient focusing: a novel method for protein separation. *Biotechnol Prog*. 1996;12:822–836.
10. Warnick KF, Francom SJ, Humble PH, Kelly RT, Woolley AT, Lee ML, Tolley HD. Field gradient electrophoresis. *Electrophoresis*. 2005;26:405–414.
11. Bird RB, Stewart WE, Lightfoot EN. *Transport Phenomena*. New York: John Wiley & Sons; 1960.
12. Newman JS. *Electrochemical Systems*. Engelwood Cliffs, NJ: Prentice-Hall, Inc; 1991.
13. Mosher RA, Saville DA, Thormann W. *The Dynamics of Electrophoresis*. New York: VCH; 1992.
14. Beretta S, Chirico G, Arosio D, Baldini G. Photon correlation spectroscopy of interacting and dissociating hemoglobin. *J Chem Phys*. 1997;106:8427–8435.
15. Ng B, Barry PH. The measurement of ionic conductivities and mobilities of certain less common organic ions needed for junction potential corrections in electrophysiology. *J Neurosci Methods*. 1995;56:37–41.
16. Lide DR, Frederikse HPR. *CRC Handbook of Chemistry and Physics*. New York: CRC Press; 1996.
17. De Bruin SH, Janssen LHM, Van Os GAJ. Study of the Bohr groups of bovine hemoglobin. *Biochim Biophys Acta*. 1969;188:207–215.
18. Douglas NG, Humffray AA, Pratt RC, Stevens GW. Electrophoretic mobilities of proteins and protein mixtures. *Chem Eng Sci*. 1995;50:743–754.
19. Bird RB, Meter DM. Turbulent Newtonian flow in annuli. *AIChE J*. 1961;7:41–45.
20. Ivory CF. Preparative free-flow electrofocusing in a vortex-stabilized annulus. *Electrophoresis*. 2004;25:360–374.
21. Giddings JC, Dahlgren K. Resolution and peak capacity in equilibrium-gradient methods of separation. *Sep Sci*. 1971;6:345–356.
22. Ettre LS. Nomenclature for chromatography. *Pure Appl Chem*. 1993;65:819–872.
23. Burke JM, Ivory CF. Characterization of voltage degradation in dynamic field gradient focusing. *Electrophoresis*. 2008;29:1013–1025.
24. Bottenus D, Leatzow D, Ivory CF. Effects of increased voltage on resolution in preparative isoelectric focusing. *Electrophoresis*. 2006;27:3325–3331.

Manuscript received May 13, 2008, and revision received Aug. 23, 2008.